

# Molecular Clouds around a Runaway O Star, $\zeta$ Ophiuchi

Kengo TACHIYARA,<sup>1,2</sup> Rihei ABE,<sup>2</sup> Toshikazu ONISHI,<sup>2</sup> Akira MIZUNO,<sup>2</sup> and Yasuo FUKUI<sup>2</sup>

<sup>1</sup>*Max-Planck-Institut für extraterrestrische Physik, Giessenbachstraße, D-85740 Garching, Germany*  
*E-mail (KT): tatihara@mpe.mpg.de*

<sup>2</sup>*Department of Astrophysics, Nagoya University, Chikusa-ku, Nagoya 464-8602*

(Received 2000 January 24; accepted 2000 June 21)

## Abstract

Molecular clouds around a runaway O star,  $\zeta$  Oph, have been surveyed with the NANTEN telescope, and their streaming motion caused by  $\zeta$  Oph has been detected.  $\zeta$  Oph is the earliest (O9.5 V) member of the Sco OB 2 association and is rapidly moving accompanied by an H II region, S 27. We detected 2 major filamentary cloud complexes, L 156 and L 204 complexes. Their total masses traced by the  $^{12}\text{CO}$  emission are  $520 M_{\odot}$  and  $1110 M_{\odot}$ , respectively. Denser molecular cloud cores detected in  $\text{C}^{18}\text{O}$  are locally distributed on the near side of the L 204 complex to  $\zeta$  Oph, and lower density gas spreads toward the opposite side. Both complexes have radial velocity shifts that are correlated with the gas density. It is suggested that the low-density gas is accelerated outward away from  $\zeta$  Oph relative to the embedded dense cores. These density and velocity structures indicate a dynamical interaction between the H II region and the molecular clouds. We calculated the kinetic energies and momenta for seven individual clouds, and examined the effects of the stellar wind and photo-evaporation by the UV field of  $\zeta$  Oph. It is found that the stellar wind can hardly input the momentum during the crossing time of the rapid movement of  $\zeta$  Oph. UV radiation seems to be a more likely origin of the streaming gas motion.

**Key words:** ISM: clouds — ISM: individual (Ophiuchus region, LDN 156, LDN 204) — ISM: kinematics and dynamics — ISM: molecule — stars: formation

## 1. Introduction

$\zeta$  Oph (HD 149757; O9.5 V type,  $\alpha_{1950} = 16^{\text{h}}34^{\text{m}}24^{\text{s}}.1$ ,  $\delta_{1950} = -10^{\circ}28'03''$ ) is the earliest star among the members of the Sco OB 2 association (de Geus et al. 1989). The bright UV and optical light of the star provide good opportunities to study the foreground diffuse interstellar medium in many emission and absorption lines of various molecules and atoms, and the chemical composition has been derived (e.g., Morton 1975; Langer et al. 1987; Kopp et al. 1996; Liszt 1997).  $\zeta$  Oph, itself, is ionizing a density-bound H II region, Sh 2–27 (S 27; Sharpless 1959), which spreads in an elliptical shape of  $\sim 7^{\circ} \times 10^{\circ}$  in  $\alpha$  and  $\delta$  (Morgan et al. 1955), corresponding to  $\sim 18 \text{ pc} \times 26 \text{ pc}$  at a distance of 140 pc. Some of the extinction features shading the  $\text{H}\alpha$  emission are seen in a plate taken by Sivan (1974), which represents the existence of dark clouds in the foreground of S 27. These features coincide with dark clouds LDN 156 (L 156; LDN is abbreviated to L hereafter), L 204, L 190, and so on (Lynds 1962); these clouds may be interacting with the H II region.

Physical interactions between early type stars and molecular clouds should be important processes related to the formation, evolution, and dissociation of molecular

clouds.  $\zeta$  Oph and its surroundings are one of the best sites to investigate these interactions because of its proximity to the sun. The distance to the star is estimated to be 200 pc (Lesh 1968), 170 pc (Bohlin 1975), and 140 pc (Draine 1986).  $\zeta$  Oph is also known as a rapidly moving runaway star, and the proper motion has been measured to be  $\mu_{\alpha*} = 0''.013 \text{ yr}^{-1}$ ,  $\mu_{\delta} = 0''.025 \text{ yr}^{-1}$  (Perryman et al. 1997). The helio-centric radial velocity of  $\zeta$  Oph is  $-10.7 \text{ km s}^{-1}$  (Lesh 1968) and the space velocity with respect to the local standard of rest (LSR) is  $3.3 \text{ km s}^{-1}$  in the radial direction,  $31.2 \text{ km s}^{-1}$  in the direction of increasing  $l$ , and  $5.0 \text{ km s}^{-1}$  in the direction of increasing  $b$  (Draine 1986).  $\zeta$  Oph, therefore, has passed through the Ophiuchus region for a few million years. This implies that the molecular clouds may have experienced being illuminated by strong UV light on a short time scale, and this provides an ideal laboratory to study the physical interactions between molecular clouds and an early type star.

McCutcheon et al. (1986) made mm-wave observations in the  $J = 1-0$   $^{12}\text{CO}$  and  $^{13}\text{CO}$  emission toward L 204, and found that the cloud has velocity structures which correlate with the spatial distribution of the bent filament. They suggested that the filamentary cloud is in-

fluenced by external compression, possibly due to  $\zeta$  Oph, resulting in the velocity structure and the morphology of the cloud. The spatial and density coverage is, however, limited, and more extensive observations with a wide-density regime are needed to reveal the dynamical interaction. They also showed that the optical polarization vectors are aligned perpendicular to the long axis of L 204, which suggests the magnetic fields penetrating the filamentary cloud perpendicularly. Heiles (1988) estimated the magnetic field strength from the H I Zeeman splitting to be  $\sim 12 \mu\text{G}$ .

Nozawa et al. (1991) made extensive  $^{13}\text{CO}$  observations covering the entire Ophiuchus North region and revealed large-scale cloud distribution. There are 3 molecular clouds identified in an area of  $\sim 10 \text{ deg}^2$  around  $\zeta$  Oph, while only one young stellar object is found to be physically associated there. They conclude that the Ophiuchus North region is inactive in star formation despite the existence of massive molecular gas of  $\sim 4400 M_{\odot}$ . Subsequently, denser gas distributions were studied by Tachihara et al. (2000) with  $\text{C}^{18}\text{O}$  observations, which found dense cloud cores whose average density is  $\sim 10^4 \text{ cm}^{-3}$  embedded in the molecular clouds.

In order to reveal the dynamical interaction in the region of  $\zeta$  Oph and to investigate how it affects the cloud structure and dynamics, we have made extensive  $^{12}\text{CO}$  molecular line observations toward the region. In section 2, we briefly summarize the observational properties and spatial and velocity distributions; the physical parameters of the detected clouds are mentioned in section 3. Section 4 discusses the dynamical interaction between  $\zeta$  Oph and the molecular clouds by introducing calculations of the kinematic energy and momentum. Finally, a summary of this paper is given in section 5.

## 2. Observations

An area of  $\sim 47 \text{ deg}^2$  around  $\zeta$  Oph and S 27 has been observed in the  $^{12}\text{CO}$  ( $J = 1-0$ ) emission line (115.2 GHz) with the NANTEN millimeter-wave telescope (HPBW =  $2'.7$ ) at Las Campanas Observatory. In total, 10575  $^{12}\text{CO}$  spectra were obtained with  $4'$  grid spacing. The velocity resolution of each spectrum is  $\sim 0.1 \text{ km s}^{-1}$ , and the velocity coverage is  $100 \text{ km s}^{-1}$ , centered at  $5 \text{ km s}^{-1}$ . The absolute antenna temperature was calibrated by adopting the peak  $T_{\text{r}}^*$  of  $\rho$  Oph East, IRAS point source 16293–2422, as 15 K. The typical integration time for each observed point was  $\sim 5 \text{ s}$ , and the rms noise temperature after the calibration was  $\sim 0.56 \text{ K}$  for  $0.1 \text{ km s}^{-1}$  velocity resolution.

To investigate the denser region of the molecular cloud, L 204 was also observed in the  $^{13}\text{CO}$  ( $J = 1-0$ ) emission line (110.20137 GHz) with the 4 m millimeter-wave telescope installed at Nagoya University; 491  $^{13}\text{CO}$  spectra were obtained with a  $4'$  grid spacing. The velocity resolu-

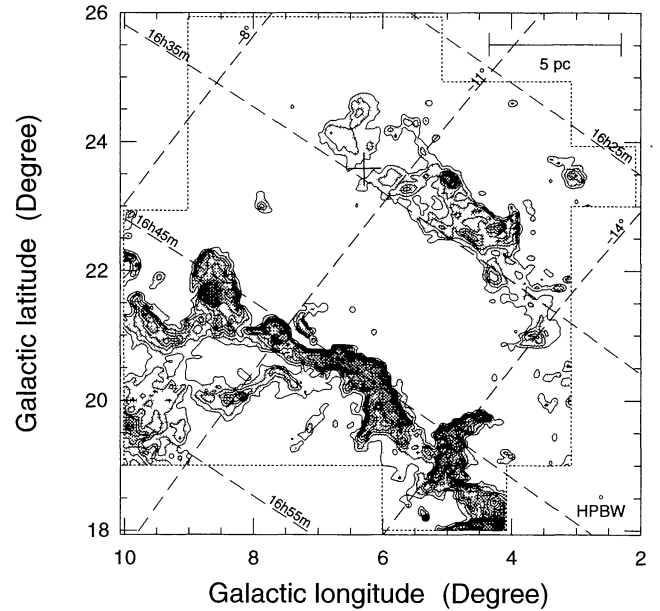


Fig. 1. Integrated intensity map of the  $^{12}\text{CO}$  ( $J = 1-0$ ) emission line in the galactic coordinates. Contours are drawn from  $1.2 \text{ K km s}^{-1}$  with  $2.4 \text{ K km s}^{-1}$  step. The dotted lines show the observed area in  $^{12}\text{CO}$ . The broken lines are grids in the equatorial coordinates (B1950). The plus mark denotes the position of  $\zeta$  Oph.

tion is the same as that mentioned above. The intensity scale of the  $^{13}\text{CO}$  spectra were calibrated while referring to  $T_{\text{r}}^*$  of M17SW as  $14.7 \text{ K}$  (Nozawa et al. 1991). In order to compare the dense cores embedded in the cloud,  $\text{C}^{18}\text{O}$  data were also obtained with the same telescope for the intense parts of the  $^{13}\text{CO}$  emission with  $2'$  grid spacing (Tachihara et al. 2000). The total number of  $\text{C}^{18}\text{O}$  spectra obtained in this region was  $\sim 940$ .

## 3. Results

### 3.1. Overview of the $^{12}\text{CO}$ Distribution

The integrated intensity of the  $^{12}\text{CO}$  ( $J = 1-0$ ) emission is shown in figure 1. Two major filamentary complexes exist, lying from the north to the south. The western one runs along  $\alpha = 16^{\text{h}}33^{\text{m}}$ , crossing through the center of the H II region with  $\sim 10\text{-pc}$  length and  $\sim 3\text{-pc}$  width. Some dark clouds including L 156, L 145, and L 121 were identified inside of this complex (hereafter L 156 complex).  $\zeta$  Oph exists at  $\sim 1^\circ$  north of the center of the L 156 complex and the  $^{12}\text{CO}$  intensity toward the star is apparently weaker than that of other parts. Another cloud complex (hereafter L 204 complex) has a curved filamentary structure of  $\sim 20\text{-pc}$  length and  $\sim 2\text{-pc}$  width as a whole, being located near to the eastern boundary of the H II region. Some  $^{12}\text{CO}$  peaks are

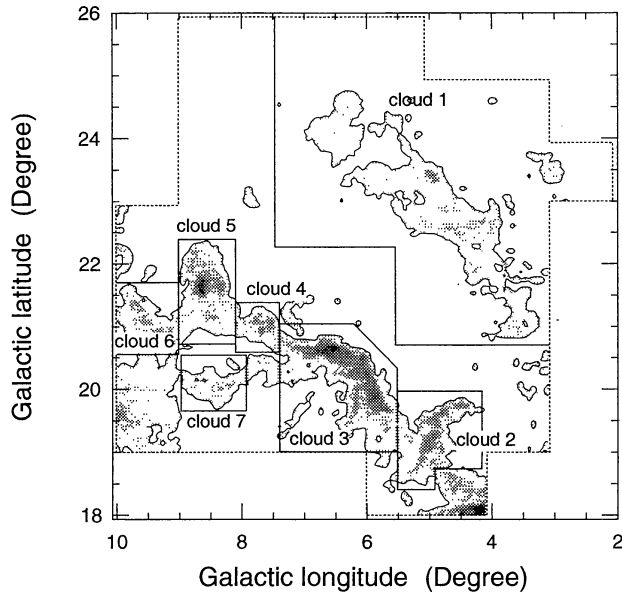


Fig. 2. Identification of the molecular clouds. The gray image is the integrated intensity of  $^{12}\text{CO}$  and the contours show the cloud boundaries. The solid lines divide the connected molecular clouds. Incompletely observed clouds are excluded. The dotted lines show the observed area in  $^{12}\text{CO}$ .

also embedded in places, being connected by filamentary clouds. Diffuse components spread toward the east of the L 204 complex. Little CO emission, however, has been detected between the 2 complexes. At the western edge of the L 204 complex, a large intensity gradient is indicated by tight contour lines, suggesting a relatively large density gradient there. The  $^{12}\text{CO}$  integrated intensity is stronger in the L 204 complex than in the L 156 complex on the whole; the strong intensity at the clumpy regions in the L 204 complex is especially prominent.

### 3.2. Physical Parameters

The L 204 complex is divided into 6 clouds bordered by less-intense bridges (see figure 2). Regarding the L 156 complex as one cloud, we estimate the physical parameters for each cloud as shown in table 1. In general, the  $^{12}\text{CO}$  ( $J = 1-0$ ) emission is optically thick. It becomes saturated when the  $\text{H}_2$  column density,  $N(\text{H}_2)$ , is larger than  $10^{21} \text{ cm}^{-2}$ , and may not reflect the actual  $N(\text{H}_2)$ . Nonetheless, we estimated the physical parameters of the  $N(\text{H}_2)$ , mass, and density using an empirical relation,  $N(\text{H}_2) = W(^{12}\text{CO}) \times 1.56 \times 10^{20} \text{ cm}^{-2}$  (Hunter et al. 1997), where  $W(^{12}\text{CO})$  is the integrated intensity of CO emission. Note that this conversion factor may change from region to region according to the circumstances. In the region with a strong UV field, the value is expected to be larger because of a higher degree of CO dissocia-

tion. Because it is very difficult to estimate the factor for each cloud, here we assume that it is uniform throughout the region. In this sense,  $N(\text{H}_2)$  and the mass give the lower-limit values. The cloud positions are defined as the peak-intensity position in galactic and equatorial coordinates (B1950). The cloud mass is derived by summing up the  $N(\text{H}_2)$  of all the observed points where  $W(^{12}\text{CO})$  is greater than  $1.2 \text{ K km s}^{-1}$  ( $= 3\sigma$ ). The total mass of the 7  $^{12}\text{CO}$  clouds is then calculated to be  $1630 M_\odot$ . The average  $N(\text{H}_2)$  is also estimated within the area where  $W(^{12}\text{CO}) \geq 1.2 \text{ K km s}^{-1}$  for each cloud. The peak  $N(\text{H}_2)$ ,  $T_r^*$ ,  $\Delta V$ , and  $V_{\text{LSR}}$  were measured at the most intense position of each cloud and  $T_r^*$ ,  $\Delta V$ , and  $V_{\text{LSR}}$  were estimated by fitting the spectral data to a single Gaussian profile. The total mass of the whole observed area, where  $W(^{12}\text{CO}) \geq 1.2 \text{ K km s}^{-1}$ , is  $2140 M_\odot$ .

### 3.3. Distribution of $^{13}\text{CO}$ Clouds and $\text{C}^{18}\text{O}$ Cores

Figure 3 represents a comparison among the distributions of the integrated intensity in  $^{12}\text{CO}$ ,  $^{13}\text{CO}$ , and  $\text{C}^{18}\text{O}$  in L 204 complex. The  $J = 1-0$   $^{13}\text{CO}$  and  $\text{C}^{18}\text{O}$  spectra generally trace relatively denser regions of  $\sim 10^3 \text{ cm}^{-3}$  and  $\sim 10^4 \text{ cm}^{-3}$ , respectively. The  $^{13}\text{CO}$  emission is distributed as 3 distinct clouds which coincide with the previously identified clouds (S, T, and U) by Nozawa et al. (1991), respectively. They are localized in the filamentary ridge of  $^{12}\text{CO}$ , where  $W(^{12}\text{CO}) \geq 8 \text{ K km s}^{-1}$ . The 3  $^{13}\text{CO}$  clouds have masses of 500, 75, and  $220 M_\odot$ , respectively. Tachihara et al. (2000) identified 8 cores in this region in  $\text{C}^{18}\text{O}$  (figure 3c). These  $\text{C}^{18}\text{O}$  cores generally have clumpy shapes. Cloud S has an arc-like structure and the  $\text{C}^{18}\text{O}$  cores are aligned on the outer edge of the arc. Cloud U has a “bullet”-like structure and the  $\text{C}^{18}\text{O}$  core is located at the “head”. The  $\text{C}^{18}\text{O}$  cores tend to be distributed relatively closely to  $\zeta$  Oph in the  $^{12}\text{CO}$  and  $^{13}\text{CO}$  clouds. Only one protostellar-like IRAS point source, 16442–0930, exists in this region, and it appears to be associated with the core u2. This suggests that star formation is taking place in the core. The densest regions in these clouds have  $N(\text{H}_2)$  of  $\sim 1.1 \times 10^{22} \text{ cm}^{-2}$  (peak position of core s5), as measured by  $\text{C}^{18}\text{O}$ .

### 3.4. Velocity Fields of the Clouds

The  $^{12}\text{CO}$  clouds show a velocity change from  $\sim -3.0 \text{ km s}^{-1}$  to  $\sim 7.8 \text{ km s}^{-1}$  and the velocity channel maps are shown in figure 4 (Plates 51 and 52). Each map shows an integrated intensity of  $^{12}\text{CO}$  with a velocity width of  $0.6 \text{ km s}^{-1}$ . Together with figure 5 (Plate 53), it is seen that the 2 complexes have different velocity components. The L 156 complex has a more negative velocity, ranging from  $-3 \text{ km s}^{-1}$  to  $1.8 \text{ km s}^{-1}$ , while the L 204 complex a more positive one from  $1.2 \text{ km s}^{-1}$  to  $7.8 \text{ km s}^{-1}$ . On the other hand, each complex has its own internal velocity structures.

Table 1. Observed properties.

Cloud number	$l$ ( $^{\circ}$ )	$b$ ( $^{\circ}$ )	$\alpha$ (1950) (hh mm ss.s)			$\delta$ (1950) ( $^{\circ}$ ' ")			Mass ( $M_{\odot}$ )	$a$ (pc)	$b$ (pc)	Mean $N(\text{H}_2)$ ( $\times 10^{21} \text{ cm}^{-2}$ )	Peak $N(\text{H}_2)$ ( $\times 10^{21} \text{ cm}^{-2}$ )	$T_{\text{a}}$ (K)	$\Delta V$ ( $\text{km s}^{-1}$ )	$V_{\text{LSR}}$ ( $\text{km s}^{-1}$ )
1 ...	5.000	23.467	16	31	56.9	-11	28	57.8	520	10.2	2.8	1.6	3.1	8.10	1.86	0.05
2 ...	4.933	19.267	16	45	38.4	-14	1	56.7	200	4.2	1.4	2.3	3.5	11.08	1.60	3.90
3 ...	6.533	20.667	16	44	36.3	-11	59	36.1	430	6.5	1.5	2.6	4.4	11.18	2.29	4.09
4 ...	7.667	20.867	16	46	26.8	-11	0	49.7	70	2.0	1.7	2.5	3.3	5.86	1.91	3.29
5 ...	8.600	21.600	16	46	2.0	-9	52	49.9	230	3.7	1.9	2.5	3.7	8.23	2.51	4.05
6 ...	9.667	21.333	16	49	12.5	-9	12	52.7	100	3.1	1.4	2.1	2.6	8.93	1.58	2.64
7 ...	8.200	20.067	16	50	17.1	-11	3	46.9	70	2.3	1.5	1.7	2.7	5.03	2.41	4.19

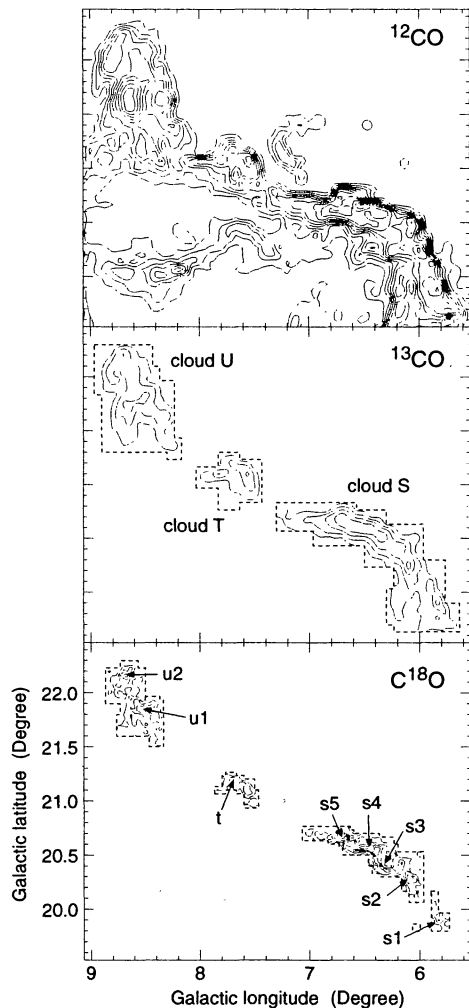


Fig. 3. Close-up images of the L 204 complex in  $^{12}\text{CO}$  (upper),  $^{13}\text{CO}$  (middle), and  $\text{C}^{18}\text{O}$  (lower). The lowest contour levels and contour intervals are  $1.2 \text{ K km s}^{-1}$  and  $2.4 \text{ K km s}^{-1}$  for  $^{12}\text{CO}$ ,  $1.6 \text{ K km s}^{-1}$  and  $1.6 \text{ K km s}^{-1}$  for  $^{13}\text{CO}$ , and  $0.18 \text{ K km s}^{-1}$  and  $0.18 \text{ K km s}^{-1}$  for  $\text{C}^{18}\text{O}$ , respectively. The observed areas in  $^{13}\text{CO}$  and  $\text{C}^{18}\text{O}$  are shown by the broken lines.  $^{13}\text{CO}$  clouds identified by Nozawa et al. (1991) and  $\text{C}^{18}\text{O}$  cores by Tachihara et al. (2000) are denoted.

First, the L 156 complex has the smallest velocity of  $-2.0 \text{ km s}^{-1}$  at the middle of the filament,  $l \simeq 4^{\circ}5$ ,  $b \simeq 22^{\circ}5$ , that is  $\sim 2^{\circ}$  south from  $\zeta$  Oph. The velocity has a gradual change to  $1 \text{ km s}^{-1}$  from this position of the apex in the velocity field to both ends of the filament.

Second, the L 204 complex has a complicated velocity structure whose peak velocity ranges from  $1.2 \text{ km s}^{-1}$  to  $7.8 \text{ km s}^{-1}$  as a whole, and each cloud has its unique velocity structure. Cloud 2 has the largest velocity of  $\sim 5 \text{ km s}^{-1}$  at the most western position (upper right in the figures) and the peak position changes to the east with the velocity decreasing down to  $\sim 2.4 \text{ km s}^{-1}$ . Cloud 3 has the largest velocity of  $\sim 5.5 \text{ km s}^{-1}$  at the position where the  $\text{C}^{18}\text{O}$  cores, s4 and s5, exist, and the intense regions change to  $\sim 1.5 \text{ km s}^{-1}$  toward both sides along the filament. Cloud 5 has a velocity structure similar to cloud 2 and has the largest velocity of  $\sim 5.4 \text{ km s}^{-1}$  at the position of the  $\text{C}^{18}\text{O}$  core, u1. A general trend can be seen in the L 204 complex, where the densest part of the cloud has the largest velocity in each cloud and smaller velocity components spread toward the less denser regions away from  $\zeta$  Oph. These features show strong indication of the dynamical interaction between molecular clouds and  $\zeta$  Oph, as discussed in section 4.

#### 4. Discussion

##### 4.1. Physical Interaction between the Clouds and $\zeta$ Oph

As shown by the morphology and velocity structure of the molecular clouds, the clouds seem to be interacting with  $\zeta$  Oph and/or its surrounding H II region. The clouds, cloud cores, and star formation are expected to be affected by  $\zeta$  Oph. It is known by previous studies that star formation is inactive around  $\zeta$  Oph, although sufficiently dense and massive clouds and cloud cores exist (Nozawa et al. 1991; Tachihara et al. 2000). Magnetic fields are suggested to play an important role for cloud dynamics (McCutcheon et al. 1986; Heiles 1988) and the turbulent energy input from  $\zeta$  Oph to the molecular clouds should be taken into account as well in considering star formation.

In order to investigate the density and temperature distributions of a cloud qualitatively, we shall compare



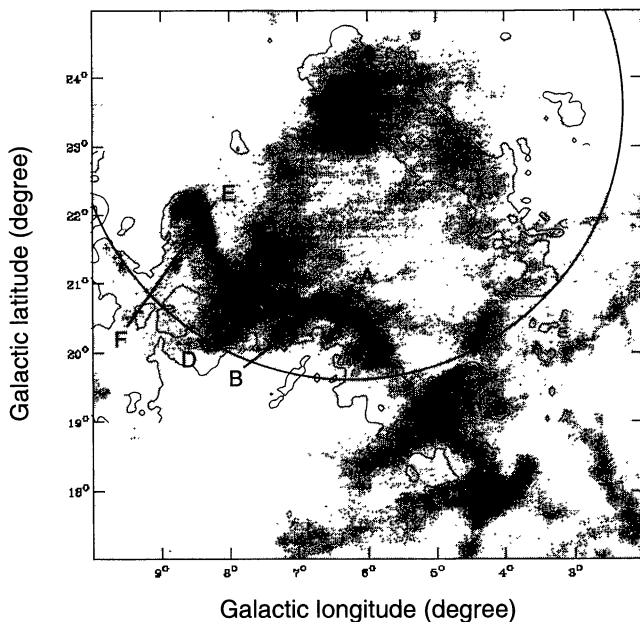


Fig. 6. Intensity map of IRAS 100  $\mu$ m. The contours of the  $^{12}\text{CO}$  cloud boundaries are overlaid. The circle shows the extent of the H II region of S 27. The three lines denote the strips where the intensity distributions are investigated (see text and figure 7).

the distributions of  $^{12}\text{CO}$ ,  $^{13}\text{CO}$ ,  $\text{C}^{18}\text{O}$ , and 100  $\mu$ m far-infrared emission. Figure 6 shows the intensity distribution of IRAS 100  $\mu$ m emission overlaid with the contour of  $^{12}\text{CO}$  clouds. We investigate the intensity distributions of the  $^{12}\text{CO}$ ,  $^{13}\text{CO}$ ,  $\text{C}^{18}\text{O}$ , and 100  $\mu$ m along 3 strip lines of A–B, C–D, and E–F illustrated by the lines in figure 6, as shown in figures 7a–c. The 3 kinds of CO distributions all show steeper gradients toward  $\zeta$  Oph.  $^{13}\text{CO}$  and  $\text{C}^{18}\text{O}$  are distributed locally close to  $\zeta$  Oph and  $^{12}\text{CO}$  spreads to the opposite sides. On the other hand, the 100  $\mu$ m peaks at the closer edge of the clouds to  $\zeta$  Oph. These features can be explained by compression of the clouds by  $\zeta$  Oph or by the surrounding H II region; denser cores are formed on the front side, and lower density gas may be accelerated to the opposite side toward the east. The front sides of the clouds facing  $\zeta$  Oph are illuminated by the UV light from  $\zeta$  Oph, and the dust temperature may increase. Thus, the 100  $\mu$ m emission is significantly enhanced on the front sides, suggesting that the gas and dust in this region may be compressed, accelerated and heated by  $\zeta$  Oph.

The 100  $\mu$ m emission is relatively weaker toward the L 156 complex than toward the L 204 complex as well as the CO intensity. The former lies on the H II region nearly across the center, while the latter lies at the boundary. The shadowing of the  $\text{H}\alpha$  emission clearly shows that

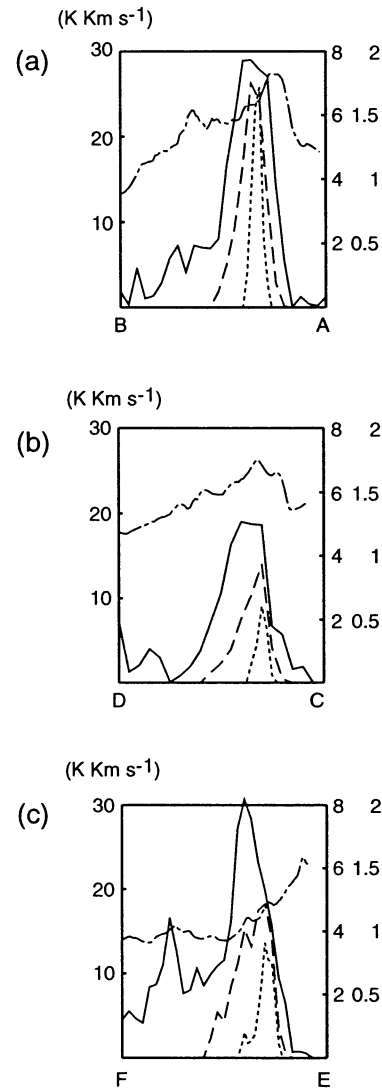


Fig. 7. Intensity distribution along the strip lines of A–B (a), C–D (b), and E–F (c). The intensity of  $^{12}\text{CO}$ ,  $^{13}\text{CO}$ ,  $\text{C}^{18}\text{O}$ , and 100  $\mu$ m are illustrated by the solid, broken, dotted, and dash-dotted lines, respectively. The intensity scales are shown in the left side ( $^{12}\text{CO}$ ) and right side ( $^{13}\text{CO}$  and  $\text{C}^{18}\text{O}$ ), while 100  $\mu$ m is an arbitrary scale.

clouds are located in front of the H II region (Sivan 1974). Because the L 204 complex has larger radial velocity and  $N(\text{H}_2)$  than does the L 156 complex, the following geometrical and kinematic structures are suggested: i.e., the 2 complexes are sheet-like molecular clouds sticking on the expanding H II region being pushed by  $\zeta$  Oph. The L 156 and L 204 complexes are face-on and almost edge-on to us, respectively, and the projection effect makes the radial velocity and  $N(\text{H}_2)$  larger for the L 204 complex. If this is the case, the smallest velocity position on the

Table 2. Kinematics of the clouds.

Cloud number	$V_1$ (km s <sup>-1</sup> )	$V_2$ (km s <sup>-1</sup> )	$P$ ( $M_\odot$ km s <sup>-1</sup> )	$E$ ( $\times 10^{45}$ erg)	$\tau_{E-SW}$ ( $\times 10^5$ yr)	$\tau_{P-SW}$ ( $\times 10^8$ yr)	$dM/dt$ ( $\times 10^{-4} M_\odot$ yr <sup>-1</sup> )	$\tau_{E-PD}$ ( $\times 10^4$ yr)	$\tau_{P-PD}$ ( $\times 10^5$ yr)
1 ...	-2.6	1.6	690	16.6	1.9	1.0	2.3	1.8	1.5
2 ...	5.2	1.6	240	4.7	2.6	1.7	2.2	0.5	0.5
3 ...	6.0	1.6	800	20.8	6.8	3.3	3.3	1.6	1.2
4 ...	4.4	1.6	60	0.9	0.9	0.8	1.5	0.2	0.2
5 ...	5.4	1.6	360	7.9	3.7	2.1	2.5	0.8	0.7
6 ...	3.8	0.8	100	1.6	1.2	0.9	1.8	0.2	0.3
7 ...	5.4	2.0	70	1.3	1.2	0.8	1.5	0.2	0.2

L 156 complex is the nearest to us. Though it is actually  $\sim 2^\circ$  south from the  $\zeta$  Oph, as mentioned above, it is explained by the rapid proper motion of  $\zeta$  Oph. About  $2.5 \times 10^5$  yr ago,  $\zeta$  Oph existed by  $\sim 30'$  closer to the position of the smallest velocity in the L 156 complex ( $l \sim 4^\circ 5$ ,  $b \sim 22^\circ 5$ ). The existence of some T Tauri stars (Nozawa et al. 1991) shows that the molecular clouds are preexistent and have formed stars prior to the passage of  $\zeta$  Oph; we now see the results of the interaction between  $\zeta$  Oph and the preexistent molecular clouds.

As mentioned in subsection 3.4, in the L 204 complex the lower density gas has a smaller radial velocity and is spread over far from  $\zeta$  Oph. This can be interpreted as molecular gas being pushed by some effects due to  $\zeta$  Oph; gas at the near side of the cloud to  $\zeta$  Oph is compressed and denser cores have been formed. Some fraction of the gas has been torn off from the cloud. The denser and more massive cloud cores can hardly be moved, while the low-density gas can easily be accelerated. It is likely that the L 204 complex had simpler velocity structures and that the gas and dust were not dynamically affected prior to the passage of  $\zeta$  Oph. Since  $\zeta$  Oph approached the clouds, the complicated velocity fields may have resulted. Around the inter-cloud region between the 2 complexes, faint string-like features in  $100 \mu\text{m}$  running nearly perpendicular to the filamentary complexes can be seen, although no CO emission is detected, perhaps due to the low column density there. These strings are also prominent in the east of the L 204 complex, as traced by the strip lines A–B, C–D, and E–F, and they are nearly parallel to the projected magnetic fields (McCutcheon et al. 1986). This suggests that some of the gas and dust has been torn off from the clouds and is flowing toward downstream along the magnetic fields.

We also note that the  $^{12}\text{CO}$  emission is significantly weak toward  $\zeta$  Oph. This may be because a large fraction of the CO molecules are dissociated by UV light. In the inter-cloud regions and cloud boundaries facing  $\zeta$  Oph, there must be photo-dissociation regions (PDRs), where CO molecules cannot be detected. This dissociation can also make the steep intensity gradients by the UV light penetrating into the cloud from the outside.  $N(\text{H}_2)$  and the cloud mass traced by CO represent the quantities only for the dense part of the molecular cloud where the

UV flux is effectively shielded by interstellar dust. In this sense, the obtained values of  $N(\text{H}_2)$  and mass should be regarded as the lower bounds, as mentioned in subsection 3.2. The observations of other tracers, like C I and C II emission, with high spatial resolutions are required to estimate the gas density in PDR more accurately.

#### 4.2. Energetics of Cloud Motion and the Origin of the Kinematic Energy Input

To understand the physical interaction between  $\zeta$  Oph and the molecular clouds quantitatively, the kinetic energy and momentum of the clouds are discussed. First, we assume that the gas component with the smallest velocity of cloud 1 and those with the largest velocity of clouds 2–7 are at rest and that the gas with the other velocity component moves away from the remaining gas due to the effects of  $\zeta$  Oph. The momentum,  $P$ , and the kinetic energy,  $E$ , are estimated for each cloud as follows:

$$P = \sum_{V=V_1}^{V_2} M_V |V - V_1|, \quad (1)$$

$$E = \frac{1}{2} \sum_{V=V_1}^{V_2} M_V (V - V_1)^2, \quad (2)$$

where  $V$  is the radial velocity, and  $M_V$  is the mass contained in the channel at  $V$ . Taking  $V_1$  and  $V_2$  as the rest velocity and the velocity of the most highly accelerated component of each cloud, respectively,  $P$  and  $E$  are obtained, as shown in table 2. The total  $P$  and  $E$  of all the clouds amount to  $2330 M_\odot$  km s<sup>-1</sup> and  $5.4 \times 10^{46}$  erg, respectively. As the dynamical effect for the compression and acceleration of the gas due to  $\zeta$  Oph, the stellar wind and UV radiation will be considered as follows.

First, the energy and momentum input by the stellar wind (SW) will be discussed. If we accept the physical parameters of the O9.5 V type  $\zeta$  Oph that the SW has  $dm/dt \simeq 10^{-7} M_\odot$  yr<sup>-1</sup> and  $V_0 \simeq 1200$  km s<sup>-1</sup> (Morton 1975), where  $dm/dt$  and  $V_0$  are the mass-loss ratio and the escape velocity, respectively, the total energy and momentum of the SW for a period of  $\tau$  yr are obtained as  $E_{\text{SW}} = \tau \times (1/2)(dm/dt)V_0^2 = \tau \times 1.5 \times 10^{42}$  [erg] and  $P_{\text{SW}} = \tau \times (dm/dt)V_0 = \tau \times 1.2 \times 10^{-4}$  [ $M_\odot$  km s<sup>-1</sup>],

respectively. We assume here that clouds are of prolate shapes with the axial lengths listed in table 1. The area exposed to the wind is then expressed as  $\pi ab$ , where  $a$  and  $b$  are the major and minor axes of the cloud, respectively. The energy and momentum input to the cloud is expressed as  $E_{\text{SW}} \times (\pi ab)/(4\pi d^2)$  and  $P_{\text{SW}} \times (\pi ab)/(4\pi d^2)$ , respectively, where  $d$  is the distance between  $\zeta$  Oph and the cloud. Thus, the expected time scales for the energy and momentum input ( $\tau_{\text{E-SW}}$  and  $\tau_{\text{P-SW}}$ , respectively) are calculated independently for each cloud, as listed in table 2.

Next, we consider the photo-dissociation effect by the UV flux of  $\zeta$  Oph. When a molecular cloud is illuminated by UV light, molecular gas will be evaporated away from the cloud with supersonic velocity, injecting momentum into the cloud. The cloud is then pushed backward as the so-called rocket effect (e.g., Oort, Spitzer 1954). The kinetic energy input by the evaporated gas is roughly calculated as follows: the number of Lyman photons radiated by  $\zeta$  Oph per each second is given as  $1.2 \times 10^{48} \text{ s}^{-1}$  (Panagia 1973). When we assume that all of the clouds are on the Strömgren sphere at  $\sim 11$  pc away from  $\zeta$  Oph, the Lyman photon flux on the cloud surface,  $J_{\text{L}}$ , is estimated to be  $8.3 \times 10^7 \text{ cm}^{-2} \text{ s}^{-1}$ . The particle density of ionized gas,  $n_{\text{i}}$ , and  $J_{\text{L}}$  have the relation

$$J_{\text{L}} = 0.01 \alpha n_{\text{i}}^2 r_{\text{i}} \frac{m_{\text{i}}^2 + 1}{m_{\text{i}}^2 - 1}, \quad (3)$$

where  $m_{\text{i}}$  is the Mach number of the streaming gas,  $r_{\text{i}}$  the spherical cloud radius, and  $\alpha$  the recombination coefficient (Kahn 1969). Here, we take  $m_{\text{i}} = 2$ ,  $\alpha = 2 \times 10^{-13}$  (Reipurth 1983) and  $r_{\text{i}}^2 = ab$ ;  $n_{\text{i}}$  can be calculated for each cloud. The mass-loss rate from a cloud hemisphere illuminated by UV is expressed as

$$\frac{dM}{dt} = \pi ab \mu_{\text{i}} n_{\text{i}} v, \quad (4)$$

where  $\mu_{\text{i}}$  and  $v$  are the particle mass ( $1.4 m_{\text{H}}$ ) and the escape velocity, respectively. If we take  $v = 20 \text{ km s}^{-1}$  according to Oort and Spitzer (1954), the mass-loss rates of the clouds are estimated as listed in table 2. By using this, the energy input by photo-dissociation can be expressed as  $E_{\text{PD}} = 1/2 (dM/dt) v^2 \tau_{\text{E-PD}}$ , where  $\tau_{\text{E-PD}}$  is the time scale of photo-dissociation; for the momentum,  $P_{\text{PD}} = (dM/dt) v \tau_{\text{P-PD}}$ . Assuming that the kinetic energy and momentum of the clouds are made only by this rocket effect, we estimate  $\tau_{\text{E-PD}}$  and  $\tau_{\text{P-PD}}$  as listed in table 2.

The above two estimations are given as lower limits for the time scales, because we assume that the momentum- and energy-transfer coefficients are 100%, the tangential velocity of the flowing gas is neglected, and the UV shielding effect by dust grains is also neglected. Nonetheless, these analyses tell us some information about the gas motion. For some of the clouds, the energy input by SW

needs a time scale,  $\tau_{\text{E-SW}}$ , of only a few  $\times 10^5$  yr or less, that is comparable with the crossing time of  $\zeta$  Oph,  $\tau_{\star}$ , through the clouds [see figure 5 (Plate 53)]. However, the time scales required for the momentum input range around  $10^8$  yr and are significantly larger than  $\tau_{\star}$ . Thus, we conclude that the stellar wind can hardly drive the high velocity gas in a relatively short timescale of  $\tau_{\star}$ . An U-shaped bow shock around  $\zeta$  Oph was found in [O III] 5010 Å and 60  $\mu\text{m}$  bands (Gull, Sofia 1979; Van Buren, McCray 1988). This seems to be a partial shocked distorted bubble which is driven by SW. The size of the bubble is expected to be smaller than a few pc, which is significantly less than the distance to the clouds, since the expansion time scale is only a few  $\times 10^5$  yr (Weaver et al. 1977). This also supports the result, because SW cannot affect the clouds penetrating through the bow shocks. On the other hand, the rocket effect by UV photo-dissociation is more likely to be the cause of the peculiar velocity structures in the cloud. The required time scales for both the kinetic energies and momenta are less than  $\tau_{\star}$  and seem to be reasonable. Here, we conclude that the rocket effect may be one of the possible mechanisms of gas acceleration.

#### 4.3. Possible Origin of Turbulence in a Molecular Cloud

Generally speaking, interstellar molecular gas is highly turbulent, as inferred from the significantly larger molecular linewidth than the thermal one. It is also a general trend that denser gas has a smaller linewidth, roughly speaking,  $\sim 10 \text{ km s}^{-1}$  for HI gas,  $\sim 2 \text{ km s}^{-1}$  for  $^{12}\text{CO}$ ,  $\sim 1 \text{ km s}^{-1}$  for  $^{13}\text{CO}$ , and  $\sim 0.5 \text{ km s}^{-1}$  for  $\text{C}^{18}\text{O}$ . Recent studies revealed that the turbulent motion of gas may play an important role in cloud dynamics and star formation (Dobashi et al. 1996; Yonekura et al. 1997; Kawamura et al. 1998; Tachihara et al. 2000). Among all, Tachihara et al. (2000) suggest that the turbulence decay may lead to a further contraction of the cloud cores. Since most of the cores in the Ophiuchus North region are starless, there must be no disturbance from YSO formed in the cores. As shown in detail by Nakano (1998), it is difficult to excite the turbulence in the cores from outside by magnetic field lines. Thus, the turbulence may be monotonically dissipated in time through the dynamical evolution of a core. If this is the case, the amount of turbulent energy of the original diffuse gas cloud and the dissipation rate of the turbulence are essential factors in core evolution. As shown in the previous section, photo-dissociation by UV light is one of the probable causes of the turbulence. Since  $\zeta$  Oph is a runaway star crossing the Ophiuchus region for about a few million years, it may have disturbed the interstellar gas and put a significant amount of turbulent energy into all of the clouds preexisting in the region during its travel. There are a few ten OB stars in the Scorpius OB 2 associa-

tion and the contribution of the rest of these OB stars should not be neglected. The field strength of the total UV radiation is estimated to be an order of magnitude larger than the typical value for the galactic plane (Nozawa et al. 1991). This may explain why star formation in the Ophiuchus North region is very inactive. de Geus (1992) and Preibish and Zinnecker (1999) present a scenario that a massive star in upper Scorpius constellation exploded as a supernova about 1.5 Myr ago. A shock wave dispersed the clouds in the vicinity of the explosion and has compressed the  $\rho$  Oph cloud core, inducing the extremely active star formation in the  $\rho$  Oph cloud core. We can see an expanding H I shell centered at  $l \sim 345^\circ$  and  $b \sim 25^\circ$ , at whose boundary the  $\rho$  Oph cloud exists (de Geus 1992). The shock wave has not, however, reached the Ophiuchus North region (Tachihara et al. 1996). When we trace the position of  $\zeta$  Oph back to 1.5 Myr ago, its former position shows good agreement with the center of the shell (de Geus 1992), which also supports the scenario that the previous companion of  $\zeta$  Oph has exploded.

## 5. Summary

A summary of this paper is as follows:

1.  $^{12}\text{CO}$  ( $J = 1-0$ ) observations around the region of  $\zeta$  Oph of  $47 \text{ deg}^2$  have revealed two major filamentary cloud complexes (L 156 and L 204 complexes) lying on the near-side of an H II region S 27.
2. These cloud complexes are divided into 7 clouds whose masses range from  $70 M_\odot$  to  $520 M_\odot$  and their total mass is  $1630 M_\odot$ .
3. The denser parts of the cloud, which are traced by  $^{13}\text{CO}$  and  $\text{C}^{18}\text{O}$  emission, are located in the filaments facing  $\zeta$  Oph and the cloud complexes have peculiar velocity structures. These imply the physical interaction of the clouds and the H II region that the molecular gas is pushed and flown away from  $\zeta$  Oph.
4. We investigate the momentum and the kinetic energy for each molecular cloud. The cloud momentum and kinetic energy range,  $60\text{--}800 M_\odot \text{ km s}^{-1}$  and  $(0.9\text{--}21) \times 10^{45} \text{ erg}$ , respectively.
5. As the origin of the streaming motion, the stellar wind from  $\zeta$  Oph and UV photo-dissociation effect are considered. The estimated time scales required for producing the momenta and kinetic energies of the clouds show that the stellar wind is hardly the cause of the gas acceleration, while UV photo-dissociation can be.
6. The turbulent cloud motion has been suggested to be an important factor for cloud evolution by previous studies. Our results indicate that photo-dissociation by a strong UV field may put the turbulent energy into the clouds and result in low star-formation activity in this region if the contribution from other members of the Scorpius OB 2 association is taken into account.

We would like to thank Ralph Neuhauser, Yoshinori Yonekura, and Nobuyuki Yamaguchi for very helpful comments on the manuscript. We greatly appreciate the hospitalities of all staff members of the Las Campanas Observatory of the Carnegie Institution of Washington. The NANTEN project is based on mutual agreements between Nagoya University and Carnegie Institution of Washington. We also acknowledge that this project could be realized by contributions from many Japanese public donors and companies. This work was financially supported in part by Grant-in-Aid for International Scientific Research from the Ministry of Education, Science, Sports and Culture of Japan (No.10044076). Two of the authors (YF and AM) acknowledge financial support from the scientist exchange program under bilateral agreement between JSPS (Japan Society for the Promotion of Science) and CONICYT (the Chilean National Commission for Scientific and Technological Research).

## References

- Bohlin R.C. 1975, *ApJ* 200, 402  
 de Geus E.J. 1992, *A&A* 262, 258  
 de Geus E.J., de Zeeuw P.T., Lub J. 1989 *A&A* 216, 44  
 Dobashi K., Bernard J.P., Fukui Y. 1996, *ApJ* 466, 282  
 Draine B.T. 1986, *ApJ* 310, 408  
 Gull T.R., Sofia S. 1979, *ApJ* 230, 782  
 Heiles C. 1988, *ApJ* 324, 321  
 Hunter S.D., Bertsch D.L., Catelli J.R., Dame T.M., Digel S.W., Esposito J.A., Fichtel C.E., Hartman R.C., Kanbach G. 1997, *ApJ* 481, 205  
 Kahn F.D. 1969, *Physica* 41, 172  
 Kawamura A., Onishi T., Yonekura Y., Dobashi K., Mizuno A., Ogawa H., Fukui Y. 1998, *ApJS* 117, 387  
 Kopp M., Gerin M., Roueff E., Le Bourlot J. 1996, *A&A* 305, 558  
 Langer W.D., Glassgold A.E., Wilson R.W. 1987, *ApJ* 322, 450  
 Lesh J.R. 1968, *ApJS* 17, 371  
 Liszt H.S. 1997, *A&A* 322, 962  
 Lynds B.T. 1962, *ApJS* 7, 1  
 McCutcheon W.H., Vrba F.J., Dickman R.L., Clemens D.P. 1986, *ApJ* 309, 619  
 Morgan W.W., Strömgren B., Johnson H.M. 1955, *ApJ* 121, 611  
 Morton D.C. 1975, *ApJ* 197, 85  
 Nakano T. 1998, *ApJ* 494, 587  
 Nozawa S., Mizuno A., Teshima Y., Ogawa H., Fukui Y. 1991, *ApJS* 77, 647  
 Oort J.H., Spitzer L. Jr 1955, *ApJ* 121, 6  
 Panagia N. 1973, *AJ* 78, 929  
 Perryman M.A.C., Lindegren L., Kovalesky J., Hoeg E., Bastian U., Bernacca P.L., Cr     M., Donati F. 1997, *A&A* 323, L49  
 Preibisch T., Zinnecker H. 1999, *AJ* 117, 2381  
 Reipurth B. 1983, *A&A* 117, 183  
 Sharpless S. 1959, *ApJS* 4, 257  
 Sivan J.P. 1974, *A&AS* 16, 163



- Tachihara K., Dobashi K., Mizuno A., Ogawa H., Fukui Y. 1996, PASJ 48, 489
- Tachihara K., Mizuno A., Fukui Y. 2000, ApJ 528, 817
- Van Buren D., McCray R. 1988, ApJ 329, L93
- Weaver R., McCray R., Castor J., Shapiro P., Moore R. 1977, ApJ 218, 377
- Yonekura Y., Dobashi K., Mizuno A., Ogawa H., Fukui Y. 1997, ApJS 110, 21

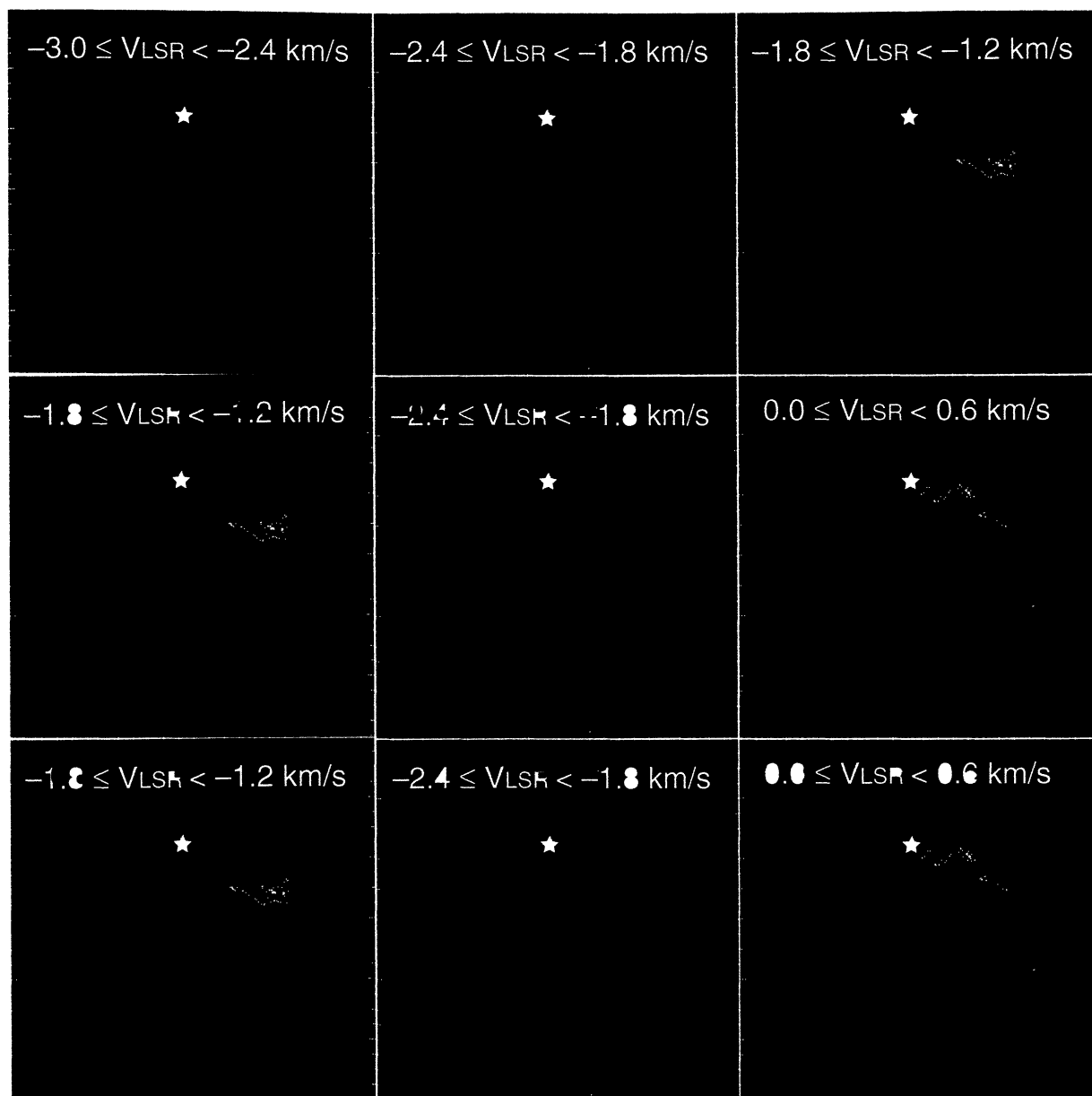


Fig. 4. Pseudo-color images of channel maps in  $^{12}\text{CO}$ . Each map is integrated over  $\Delta V = 0.6 \text{ km s}^{-1}$ . The integrated velocity ranges are shown in each map. The star in each map shows the position of  $\zeta \text{ Oph}$ .

K. TACHIYARA et al. (See Vol. 52, 1149)

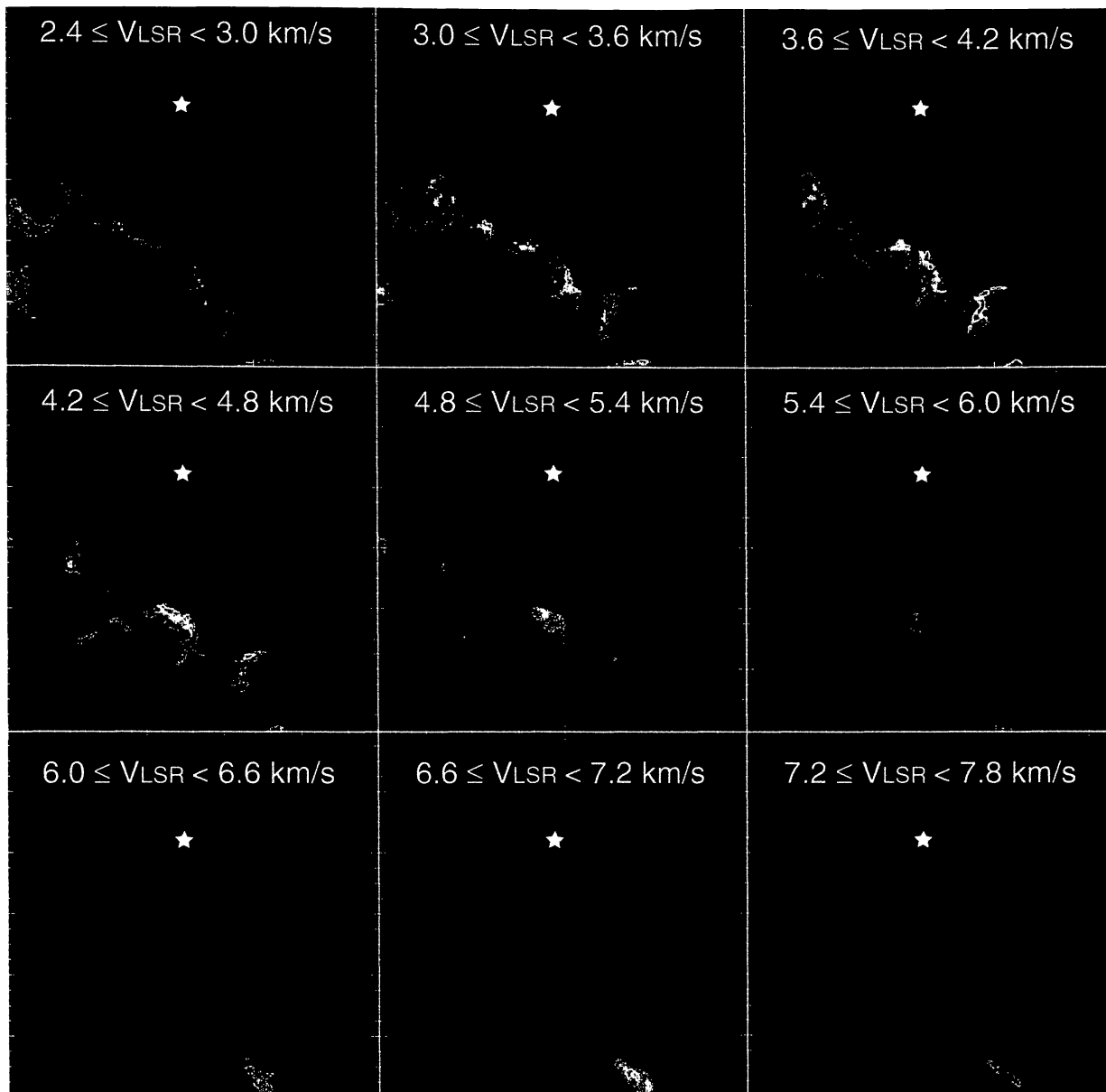


Fig. 4. (Continued.)

K. TACHIHARA et al. (See Vol. 52, 1149)

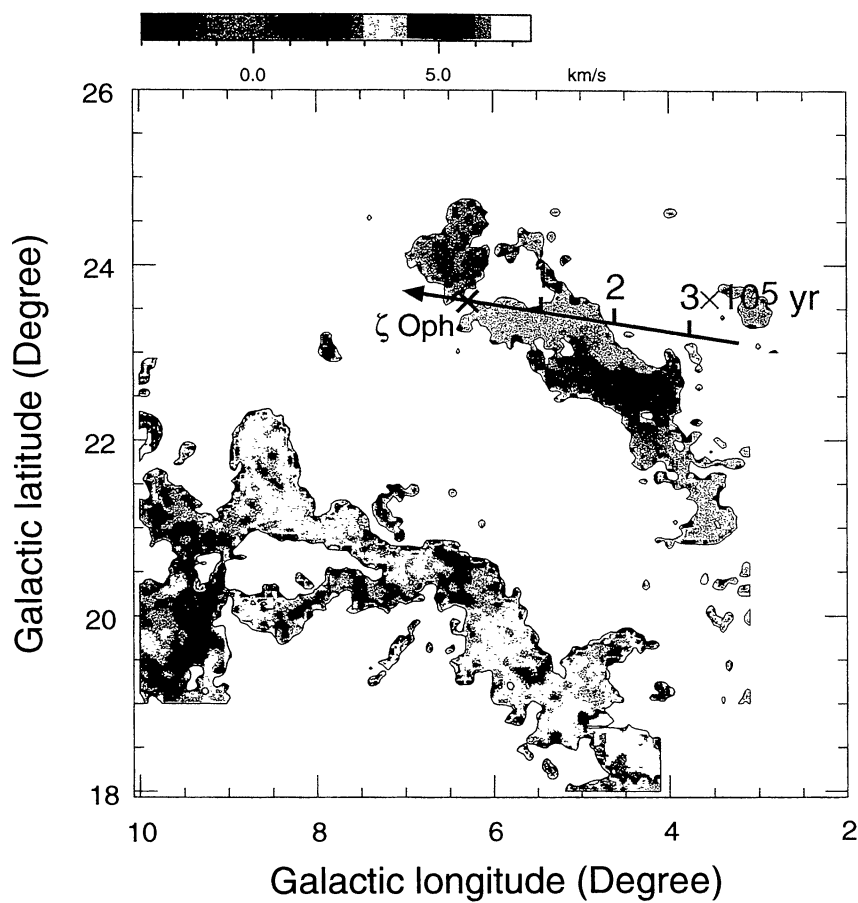


Fig. 5. Pseudo-color image of the peak velocity of  $^{12}\text{CO}$  emission. The cross mark and arrow show the position and proper motion of  $\zeta$  Oph, respectively.

K. TACHIARA et al. (See Vol. 52, 1149, 1153)